

Discovery of transient topological crystalline order in optically driven SnSe

Masataka Mogi^{1,2,*}, Dongsung Choi^{3,4,*}, Kyoung Hun Oh¹, Diana Golovanova⁵, Yufei Zhao⁵,
Yifan Su¹, Zongqi Shen¹, Doron Azoury¹, Haoyu Xia¹, Batyr Ilyas¹, Tianchuang Luo¹,
Noriaki Kida^{6,7}, Taito Osaka^{6,7}, Tadashi Togashi^{6,7}, Binghai Yan⁵ & Nuh Gedik¹✉

¹Department of Physics, Massachusetts Institute of Technology, Cambridge, MA, USA.

²Department of Applied Physics, University of Tokyo, Bunkyo-ku, Tokyo, Japan.

³Department of Electrical Engineering and Computer Science, Massachusetts Institute of
Technology, Cambridge, MA, USA.

⁴Max Planck Institute for the Structure and Dynamics of Matter, Hamburg, Germany.

⁵Department of Condensed Matter Physics, Weizmann Institute of Science, Rehovot, Israel.

⁶RIKEN SPring-8 Center, Sayo, Hyogo, Japan.

⁷Japan Synchrotron Radiation Research Institute, Sayo, Hyogo, Japan.

*These authors contributed equally: Masataka Mogi, Dongsung Choi.

✉e-mail: gedik@mit.edu

Ultrafast optical excitation of quantum materials has opened new frontiers for transiently inducing novel phases of matter¹, including magnetism², charge density waves³, ferroelectricity^{4,5}, and superconductivity⁶ beyond the constraints of equilibrium thermodynamics. Triggering a transient topological order in a trivial semiconductor represents a key milestone, as it could provide an on-demand route to topological functionality for device applications. However, achieving a topologically nontrivial phase from a large-gap (~ 1 eV) semiconductor remains a major challenge, as substantial energy modification is required to invert the band gap. Here, we report the discovery of a thermally inaccessible, transient topological crystalline order in a sizable-gap (~ 0.8 eV) layered semiconductor, SnSe, through femtosecond above-gap excitation. Time- and angle-resolved photoemission spectroscopy reveals a Dirac-like linear dispersion forming within the band gap on a subpicosecond timescale. This transient state shows hallmark features of a reflection-invariant topological crystalline insulator⁷, including a high Fermi velocity (2.5×10^5 m/s), multiple Dirac points located away from high-symmetry momenta, and independence from probe photon energy, persisting for several picoseconds even at room temperature. Our findings establish a nonequilibrium pathway to ultrafast topological order in a semiconductor, opening new avenues for optically driven spintronic and quantum information technologies.

Topological phases, featuring symmetry-protected edge and surface states, have been a central topic in condensed matter physics, with promising applications in spintronics and quantum information^{8,9}. Over the past decades, equilibrium studies of materials such as bismuth chalcogenides and IV-VI semiconductors have been pivotal in unveiling these exotic states, where band topology is primarily dictated by spin-orbit coupling and time-reversal or crystal symmetry¹⁰. Yet, access to new topological states often hinges on symmetry modifications or

band inversions that are energetically costly under thermodynamic constraints¹¹. This limitation highlights a key challenge: while equilibrium approaches have led to the discovery of many topological materials, they inherently depend on the thermodynamic stability of crystal structures, making it difficult to access phases that require significant symmetry changes or band inversions.

Nonequilibrium approaches offer an alternative route to realizing topological phases by dynamically reshaping crystal symmetries and electronic configurations beyond equilibrium limits. Methods such as epitaxial strain engineering^{12,13}, quenching into metastable states¹⁴, and laser irradiation¹⁵ have been explored as means to access otherwise inaccessible states. Among these, ultrafast optical excitation stands for its ability to drive a system into transient high-energy configurations on femtosecond timescales, enabling rapid manipulation of crystal symmetry and electronic band topology¹⁶ (Fig. 1a,b). Previous studies have demonstrated that ultrafast structural transitions can suppress or modify topological states in materials such as WTe₂ (ref. ¹⁷), MoTe₂ (ref. ¹⁸), ZrTe₅ (refs. ^{19,20}), and Bi-doped (Pb,Sn)Se (ref. ²¹). However, whether ultrafast excitation can actively induce topologically nontrivial order in a trivial semiconductor - rather than simply modifying an existing topological state – remains an open question, particularly in large-gap materials where band topology is robust against perturbations.

To explore this, we focus on SnSe, a layered IV-VI semiconductor with a sizable (~0.8 eV) band gap²². At ambient conditions, SnSe crystallizes in an orthorhombic Pnma phase (Fig. 1c), where puckered Sn-Se bilayer stacking, driven by stereochemically active Sn 5s lone-pair orbitals²³, breaks mirror symmetry, yielding a trivial insulating state. Above ~800 K, it transitions to a higher-symmetry Cmcm phase^{24–26} (Fig. 1d), which is known for high thermoelectric performance^{22,23}, but remains topologically trivial due to persistent lone-pair orbitals pointing normal to the bilayers.

Recent studies have shown that nonequilibrium methods can unlock topological phases in SnSe. Epitaxial growth on $\text{Bi}_2\text{Se}_3(111)$ ^{12,13,27} stabilizes SnSe in a cubic rocksalt structure, analogous to $(\text{Pb}_{1-x}\text{Sn}_x)\text{Se}$ ($x \leq 0.4$), a prototype topological crystalline insulator (TCI)²⁸⁻³⁰. More intriguingly, an ultrafast diffraction study indicated that femtosecond laser excitation might drive SnSe toward a rocksalt-like Immm phase³¹. This phase is characterized by shear-like atomic displacements opposite the Cmc \bar{m} phase transition (Fig. 1e), restoring mirror symmetry crucial for Dirac-like surface states. Unlike the epitaxial approach, laser excitation can transiently overcome energy barriers associated with lattice distortions, potentially reaching topological phases on subpicosecond timescales. Although recent theories^{32,33} suggest the feasibility of inducing a transient TCI state in SnSe, direct evidence of such topological behavior has remained elusive³⁴⁻³⁷. Here, by combining density functional theory (DFT) calculations and femtosecond time- and angle-photoemission spectroscopy (trARPES) with near-infrared laser excitation (100 fs, 1.55 eV), we provide direct evidence that ultrafast optical excitation induces Dirac-like surface states supported by nonzero mirror Chern numbers. This transient state emerges within the band gap on subpicosecond timescales - even at room temperature - demonstrating a robust topological crystalline order not achievable under equilibrium conditions.

Lattice and electronic structures

To elucidate the electronic properties of the transient Immm phase, we performed DFT calculations using the orthorhombic lattice parameters at ambient conditions, under the assumption that the lattice size does not vary within a few picoseconds after excitation. The calculated band structures for the (100) surface planes of the Pnma, Cmc \bar{m} , and Immm phases are shown in Fig. 1g-i. In the Pnma phase (Fig. 1g), the lack of mirror symmetry results in a sizable band gap (~ 0.8 eV), consistent with its trivial insulating nature. The Cmc \bar{m} phase (Fig.

1h), despite its higher symmetry, remains a gapped (~ 0.4 eV), topologically trivial state. In stark contrast, the hypothetical Immm phase (Fig. 1i) displays dramatically altered band structures with multiple gapless crossings near the \bar{Y} and \bar{Z} points.

In this Immm phase, our calculations identify four gapless Dirac cones in the first Brillouin zone on the (100) surface, each exhibiting linear dispersion with Fermi velocities of $\sim 2.5 \times 10^5$ m/s. Unlike time-reversal-invariant topological insulators^{8,9,38}, where Dirac cones are typically found at high-symmetry points such as $\bar{\Gamma}$ or \bar{X} , the Immm phase symmetry allows these cones to emerge away from such points, resembling the behavior of other TCI materials in the (Pb,Sn)Se family²⁸⁻³⁰. Furthermore, calculated mirror Chern numbers confirm that these Dirac points remain robustly gapless as long as the mirror symmetry is preserved. This unique gapless band structure sets the Immm phase apart from the gapped equilibrium phases (Pnma and Cmcm), highlighting the feasibility of probing topologically nontrivial states in SnSe with trARPES.

Ultrafast observation of transient in-gap band dispersion

We performed trARPES measurements on 50-nm-thick SnSe(100) films epitaxially grown on InP(100) (sample #1). Using 10.8 eV extreme ultraviolet (XUV) probe pulses³⁹, we accessed the electronic states around the \bar{Y} and \bar{Z} points in the two-dimensional Brillouin zone^{35,40} (Fig. 1f), determined based on the orthorhombic lattice constants ($a = 11.5$ Å, $b = 4.19$ Å, $c = 4.39$ Å) (Supplementary Section 1). Figure 2a shows constant energy cuts of the photoemission intensity below the Fermi level (E_F) before the arrival of the pump pulse. As expected for an intrinsic semiconductor, the intensity near E_F is nearly absent, reflecting its insulating nature of SnSe in the Pnma phase.

Upon femtosecond above-gap photoexcitation (1.55 eV, 100 fs pulse width) at a nominal absorbed fluence of 0.4 mJ/cm², we observe a significant increase in photoemission

intensity inside the nominal band gap of SnSe, as shown in Fig. 2b (pump-probe delay of 0.6 ps). Crucially, this in-gap signal lies below E_F , ruling out photoexcited carriers above the conduction band minimum as its origin³⁵. The effect is most prominent near the \bar{Z} point along the $\bar{\Gamma} - \bar{Z}$ direction. Energy-momentum snapshots at various pump-probe delays shown in Fig. 2c reveal the ultrafast emergence of a transient band with negative group velocity ($\partial E/\partial k_z < 0$), exhibiting a velocity of $\sim 2.5 \times 10^5$ m/s. This value is comparable to Dirac-like carriers in established topological systems such as Bi_2Se_3 ($\sim 5 \times 10^5$ m/s, ref. ³⁸) and SnTe ($\sim 3 \times 10^5$ m/s, ref. ³⁰). The band appears within 0.2 ps, reaches maximum intensity at ~ 0.6 ps, and decays over ~ 5 ps. Reproducibility was confirmed across multiple SnSe films, and these features were observed to persist up to room temperature (Supplementary Section 2).

The observed picoseconds transient state is distinct from Floquet-Bloch states or laser-assisted photoemission^{35,41}, which are typically observed only during the temporal overlap between pump and probe pulses, and from extrinsic effects such as surface photovoltage⁴², which typically occur on hundred picoseconds timescales. Additionally, the highly dispersive nature of the band below E_F is incompatible with defect states or localized mid-gap states, which would manifest as nondispersive features and preexist without optical excitation. Further exclusion of alternative possibilities is discussed in Supplementary Section 6. Given the absence of in-gap states in the fully gapped Cmcm phase (Fig. 1h), these results strongly indicate the formation of a genuine, non-thermal transient phase in SnSe.

Evidence for transient topological crystalline order

To verify the topological nature of the transient in-gap band, we examined its dispersion and momentum-space location in greater detail. Curvature analysis⁴³ of the trARPES data (Fig. 3a, right panel) clearly resolves a linearly dispersive feature consistent with a Dirac-like state. This linear dispersion is observed along both $\bar{\Gamma} - \bar{Z}$ (Fig. 3a) and $\bar{\Gamma} - \bar{Y}$ (Fig. 3b) directions,

showing the presence of multiple Dirac cones in the Brillouin zone. Complementary measurements using a higher probe photon energy (21.6 eV) on a SnSe film grown on a PbSe(100) buffer layer (sample #2) provides crucial additional evidence. Despite a slight chemical potential shift relative to the earlier data (Figs. 2 and 3a,b), the sample quality remained comparable (Supplementary Section 1). Accessibility to a larger momentum by the higher photon energy allowed us to observe the positive group-velocity branch ($\partial E/\partial k_z > 0$), revealing a Dirac point around $k \approx 0.92 \text{ \AA}^{-1}$ in the second Brillouin zone (Fig. 3c). This location, while unexpected because the bands usually appear also in the first Brillouin zone, proved consistent across measurements using different probe photon energies (Fig. 3d).

In contrast to the three-dimensional bulk valence bands, which exhibit moderate changes in dispersive features with varying photon energy⁴⁰, these Dirac-like bands remain pinned at the same momentum-space location, suggesting a surface origin. The absence of Dirac bands in the first Brillouin zone can be understood through matrix element effects, similar to those observed in the related TCI material $(\text{Pb}_{1-x}\text{Sn}_x)\text{Se}$ ($x = 0.23$). In $(\text{Pb},\text{Sn})\text{Se}$, trARPES measurements reveal a double-cone structure where one Dirac branch is significantly suppressed due to the matrix element effects³⁰ (Fig. 3d, inset). This observation suggests that SnSe likely hosts a similar double-cone structure (Fig. 3e), with the inner cone becoming unresolved at our photon energies (10.8 eV and 21.6 eV).

Our experimental findings align very well with theoretical predictions. Surface-state calculations for the Immm phase predict four Dirac cones distributed around the \bar{Y} and \bar{Z} points (Figs. 1i, 3f), consistent with both the observed dispersion and momentum-space location of the Dirac bands. A particularly notable feature is the Dirac point's displacement of $\sim 0.20 \text{ \AA}^{-1}$ from the zone boundary, substantially larger than the $\sim 0.08 \text{ \AA}^{-1}$ shift observed in $(\text{Pb},\text{Sn})\text{Se}$. This enhanced displacement aligns with trends seen in $(\text{Pb},\text{Sn})\text{Te}$, where increasing Sn content progressively shifts the Dirac point away from the zone boundary⁴⁴ (Supplementary

Section 3). These comprehensive measurements and analyses demonstrate that the transient phase of SnSe exhibits the hallmarks of surface states of a TCI.

Discussion and outlook

Our discovery of ultrafast, photoinduced topological order in SnSe represents a major advance in accessing quantum states of matter. We observe the emergence of Dirac-like in-gap states on subpicosecond timescales, persisting at room temperature, far beyond the reach of conventional methods that usually rely on chemical doping. This result not only uncovers a new topological state in SnSe but also sheds light on the structural and electronic dynamics that drive this nonequilibrium transformation.

Previous time-resolved X-ray diffraction (trXRD) experiments at absorbed fluences of ~ 2.2 mJ/cm² hinted that SnSe can be driven toward a higher-symmetry phase^{31,45}, yet diffraction evidence for a complete transition to the Immm structure remains elusive³⁶. To look for this, we performed our own trXRD measurements at fluences up to ~ 1.74 mJ/cm². Similar to the earlier measurements, our results show no clear signature (Supplementary Section 4), implying that any structural transition is either partial or unrealized. In contrast, trARPES combined with DFT (Supplementary Section 5) suggests a more granular view of local symmetry changes: the Dirac band position remains fixed regardless of pump fluence or time delay (Figs. 2c, 3d, Extended Data Fig. 1a,e-g), excluding a gradual, uniform distortion. Instead, Dirac-like bands appear suddenly in localized regions, implying that Immm-like domains form within a background Pnma phase. Such spatially inhomogeneous switching, where microscopic domains shape the overall response, resembles subthreshold transitions reported in correlated systems like VO₂ (ref. ^{46,47}) and charge density wave systems³, where local order develops before any evidence of fully established global phase is observed.

On a microscopic level, our results highlight the key role of photoexcited electron

depletion from lone-pair orbitals formed by hybridized Sn 5s and Se 4p_x states^{23,31}. By disturbing the stereochemical activity that sustains the puckered bilayer, this depletion temporarily stabilizes a high-symmetry lattice through enhanced σ -bonding among Sn and Se p-orbitals⁴⁸. The picosecond lifetime of this phase accords with electron-hole photoinjection dynamics and subsequent phonon-driven reorganization (Extended Data Fig. 1b,c). This behavior is further supported by the linear scaling of the in-gap band intensity with pump fluence (Extended Data Fig. 1c,d).

Our findings show the potential of nonequilibrium routes to generate transient topological orders in semiconductors with sizable gaps. There exist several tuning knobs that might extend the lifetime or improve the spatial uniformity of these phases in the future: increasing pump fluence beyond current damage threshold limitations³⁷, engineering substrate strain^{12,13}, or introducing Te/Pb dopants that foster higher-symmetry structures^{29,44}. More broadly, this work demonstrates that photoinduced symmetry restoration in layered semiconductors opens new opportunities for on-demand topological control at room temperature. We speculate that similar approaches could be adapted to a variety of materials⁴⁸, thus broadening the scope of quantum device engineering.

Acknowledgments

We are grateful to Yijing Huang, Kenji Yasuda, and Ilya Belopolski for insightful discussions. We are also thankful to Bryan Fichera and Honglie Ning for discussions about trXRD data analysis. This work was supported by the US Department of Energy, BES DMSE (data taking, analysis and manuscript writing), and Gordon and Betty Moore Foundation's EPiQS Initiative Grant No. GBMF9459 (instrumentation). M.M. is supported by JST PRESTO Grant No. JPMJPR23HA and JSPS KAKENHI Grant No. JP24K16986. N.K. is supported by JSPS KAKENHI Grant No. JP23K26157. The trXRD experiments were performed at the BL3 of

SACLA with the approval of the Japan Synchrotron Radiation Research Institute (JASRI)
Proposal No. 2024A8006.

Author contributions

N.G. supervised the project. M.M., D.C. and K.H.O. conceived the study. M.M. and D.C. grew and characterized the samples with help of H.X. M.M. and D.C. performed trARPES measurements and analyzed the data with help of H.X., D.A., and Y.S. D.G., Y.Z. and B.Y. performed DFT calculations, analyzed and interpret the data. D.C., K.H.O., M.M., Z.S., and Y.S. conducted trXRD measurements and analyzed the data with help of N.K., T.O. and T.T. B.I. and T.L. performed time-resolved reflectivity measurements and analyzed the data. M.M., D.C. and N.G. interpreted the results and wrote the manuscript with inputs from B.Y. and all other authors.

Competing interests

The authors declare no competing interests.

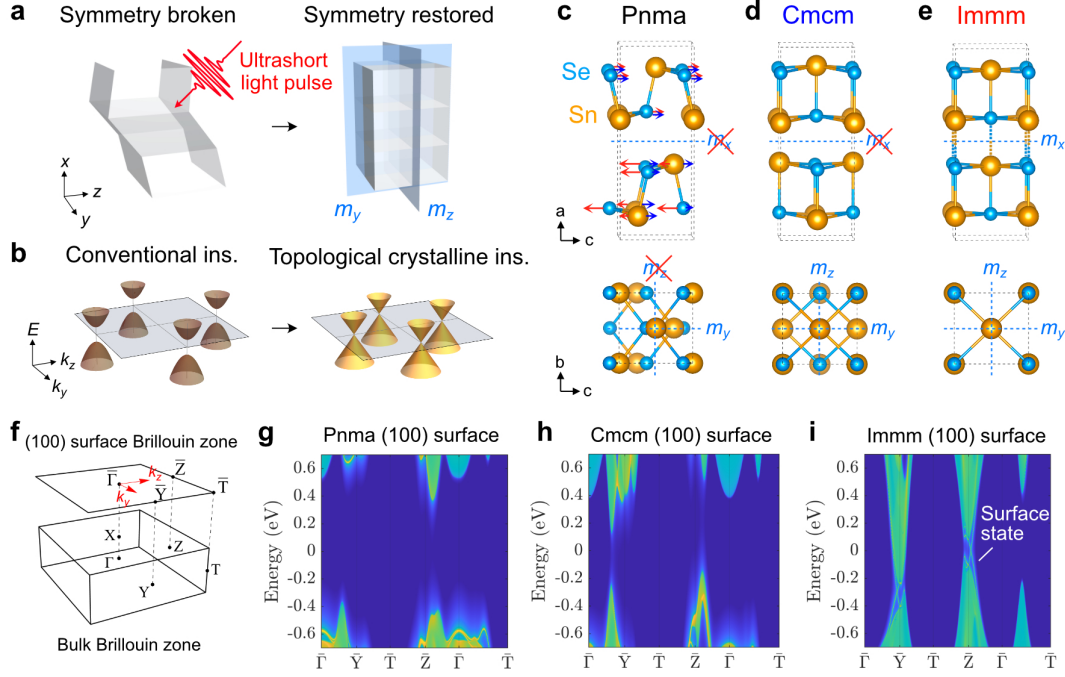


Fig. 1 | Crystal structure, band topology, and pathway for light-induced topological crystalline order in SnSe. **a**, Schematic illustration of a photo-induced structural phase transition from a lattice-distorted state to a symmetry-restored state with mirror planes of m_y and m_z . **b**, Band structure illustration showing that lattice distortion opens a gap, resulting in a topologically trivial insulating state, while photoexcitation restoring symmetry enables topological crystalline order. **c-e**, Crystal structures of SnSe viewed along b -axis (top) and a -axis (bottom) for orthorhombic space groups Pnma (**c**), Cmcm (**d**), and Immm (**e**). The lattice parameters are fixed at $a = 11.5 \text{ \AA}$, $b = 4.19 \text{ \AA}$, and $c = 4.39 \text{ \AA}$. The Pnma phase lacks a mirror plane (m_z), whereas the Cmcm and Immm phases possess mirror planes m_y and m_z . Arrows indicate the atomic displacements associated with transitions to the Cmcm (blue) and Immm (red) phases. **f**, Bulk and projected surface Brillouin zones of the primitive orthorhombic lattice, with key symmetry points and axes relevant to this study. **g-i**, Calculated band structures at the (100) surface for the Pnma (**g**), Cmcm (**h**), and Immm (**i**) phases. Unlike the Pnma and Cmcm phases, the Immm phase hosts gapless surface states characteristic of a TCI.

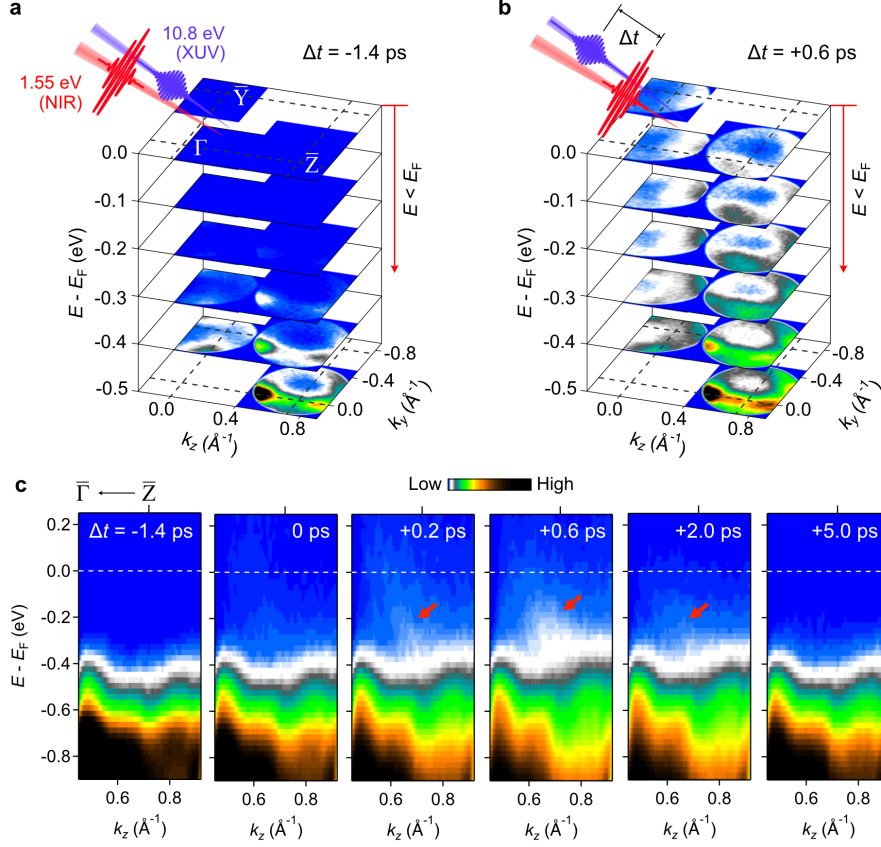


Fig. 2 | Emergence of a transient in-gap band dispersion. **a,b**, Constant-energy cuts of trARPES intensity around the $\bar{\Gamma}$ and \bar{Z} points on the (100) surface of a SnSe film (sample #1). Measurements were taken at $\Delta t = -1.4$ ps before photoexcitation (**a**) and $\Delta t = 0.6$ ps after photoexcitation (**b**) with near-infrared (NIR, 1.55 eV) incident pump fluence of 1.0 mJ cm^{-2} . Dashed lines represent the boundaries of the surface Brillouin zone. **c**, Energy-momentum snapshots along k_z at $k_y = 0 \text{ \AA}^{-1}$ near the \bar{Z} point at various time delays. The appearance of an in-gap band dispersion is highlighted by red arrows.

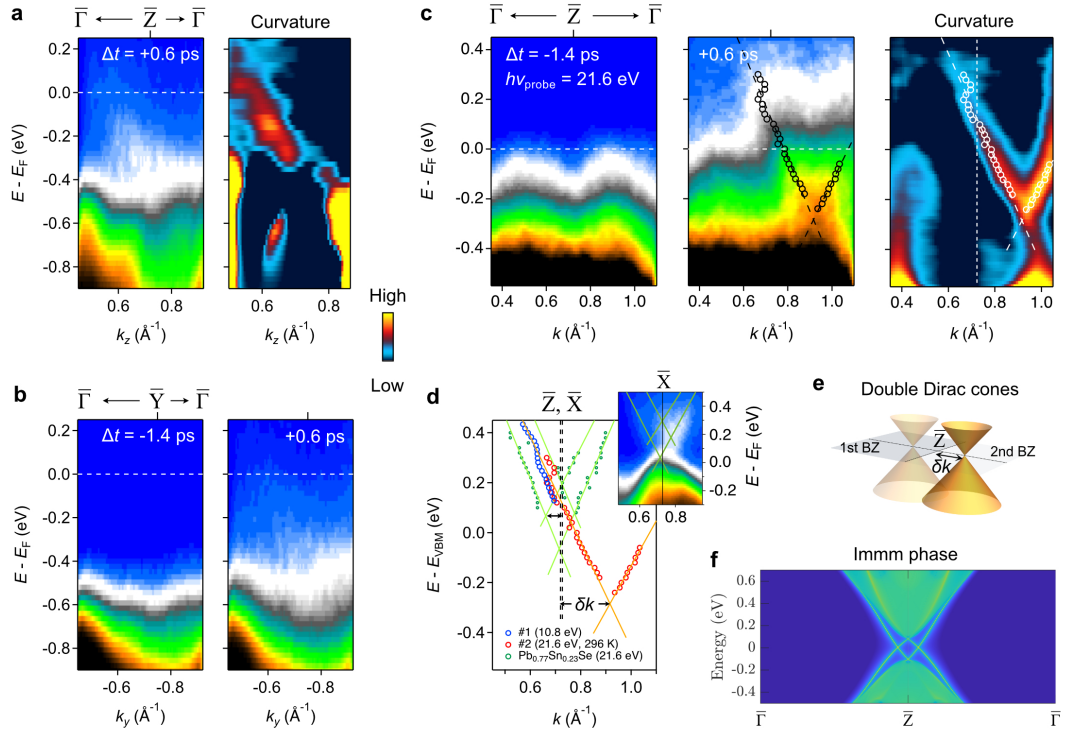


Fig. 3 | Evidence of topological crystalline order. **a**, trARPES energy-momentum cut (left) and curvature-filtered map (right) along k_z at $k_y = 0 \text{ \AA}^{-1}$ around the \bar{Z} point on the (100) surface of the SnSe film (sample #1). Measurements were taken at $\Delta t = 0.6 \text{ ps}$ with an incident pump fluence of 1.6 mJ cm^{-2} . **b**, trAPRES map around the \bar{Y} point along k_y at $k_z = 0.72 \text{ \AA}^{-1}$, measured at $\Delta t = -1.4 \text{ ps}$ (left) and $\Delta t = 0.6 \text{ ps}$ (right). **c**, trARPES map around the \bar{Z} point on the (100) surface (sample #2), using a probe photon energy of $h\nu_{\text{probe}} = 21.6 \text{ eV}$. The left and middle panels correspond to measurements at $\Delta t = -1.4 \text{ ps}$ and $\Delta t = 0.6 \text{ ps}$, respectively. The right panel shows the curvature-filtered map for $\Delta t = 0.6 \text{ ps}$. **d**, Band dispersion extracted from curvature-filtered maps. Red and blue circles indicate dispersions measured with probe photon energies of 10.8 eV and 21.6 eV , respectively. Green circles represent the dispersion for $\text{Pb}_{0.77}\text{Sn}_{0.23}\text{Se}$ in the TCI phase (inset). Solid lines show linear fits to the dispersions. **e**, Schematic of the electronic structure of a TCI with mirror planes m_y and m_z . Surface Dirac cones are located around the \bar{Y} and \bar{Z} points on the (100) surface. **f**, Focused view of the electronic structure around the \bar{Z} point. Two Dirac cones appear across the \bar{Z} point along the $\bar{\Gamma} - \bar{Z}$ direction, separated by a momentum δk . The Dirac cone in the second Brillouin zone is highlighted to illustrate the matrix element effect. **g**, DFT-calculated surface band of the Immm phase around the \bar{Z} point.

References

1. Basov, D. N., Averitt, R. D. & Hsieh, D. Towards properties on demand in quantum materials. *Nat. Mater.* **16**, 1077–1088 (2017).
2. Radu, I., Vahaplar, K., Stamm, C., Kachel, T., Pontius, N., Dürr, H. A., Ostler, T. A., Barker, J., Evans, R. F. L., Chantrell, R. W., Tsukamoto, A., Itoh, A., Kirilyuk, A., Rasing, T. & Kimel, A. V. Transient ferromagnetic-like state mediating ultrafast reversal of antiferromagnetically coupled spins. *Nature* **472**, 205–208 (2011).
3. Kogar, A., Zong, A., Dolgirev, P. E., Shen, X., Straquadine, J., Bie, Y.-Q., Wang, X., Rohwer, T., Tung, I.-C., Yang, Y., Li, R., Yang, J., Weathersby, S., Park, S., Kozina, M. E., Sie, E. J., Wen, H., Jarillo-Herrero, P., Fisher, I. R., Wang, X. & Gedik, N. Light-induced charge density wave in LaTe₃. *Nat. Phys.* **16**, 159–163 (2020).
4. Nova, T. F., Disa, A. S., Fechner, M. & Cavalleri, A. Metastable ferroelectricity in optically strained SrTiO₃. *Science* **364**, 1075–1079 (2019).
5. Li, X., Qiu, T., Zhang, J., Baldini, E., Lu, J., Rappe, A. M. & Nelson, K. A. Terahertz field-induced ferroelectricity in quantum paraelectric SrTiO₃. *Science* **364**, 1079–1082 (2019).
6. Mitrano, M., Cantaluppi, A., Nicoletti, D., Kaiser, S., Perucchi, A., Lupi, S., Di Pietro, P., Pontiroli, D., Riccò, M., Clark, S. R., Jaksch, D. & Cavalleri, A. Possible light-induced superconductivity in K₃C₆₀ at high temperature. *Nature* **530**, 461–464 (2016).
7. Fu, L. Topological Crystalline Insulators. *Phys. Rev. Lett.* **106**, 106802 (2011).
8. Hasan, M. Z. & Kane, C. L. Colloquium: Topological insulators. *Rev. Mod. Phys.* **82**, 3045–3067 (2010).
9. Qi, X.-L. & Zhang, S.-C. Topological insulators and superconductors. *Rev. Mod. Phys.* **83**, 1057–1110 (2011).
10. Wieder, B. J., Bradlyn, B., Cano, J., Wang, Z., Vergniory, M. G., Elcoro, L., Soluyanov, A. A., Felser, C., Neupert, T., Regnault, N. & Bernevig, B. A. Topological materials discovery from crystal symmetry. *Nat. Rev. Mater.* **7**, 196–216 (2022).
11. Bao, C., Tang, P., Sun, D. & Zhou, S. Light-induced emergent phenomena in 2D materials and topological materials. *Nat. Rev. Phys.* **4**, 33–48 (2022).
12. Wang, Z., Wang, J., Zang, Y., Zhang, Q., Shi, J.-A., Jiang, T., Gong, Y., Song, C.-L., Ji, S.-H., Wang, L.-L., Gu, L., He, K., Duan, W., Ma, X., Chen, X. & Xue, Q.-K. Molecular Beam Epitaxy-Grown SnSe in the Rock-Salt Structure: An Artificial Topological Crystalline Insulator Material. *Adv. Mater.* **27**, 4150–4154 (2015).
13. Jin, W., Vishwanath, S., Liu, J., Kong, L., Lou, R., Dai, Z., Sadowski, J. T., Liu, X., Lien,

- H.-H., Chaney, A., Han, Y., Cao, M., Ma, J., Qian, T., Wang, S., Dobrowolska, M., Furdyna, J., Muller, D. A., Pohl, K., Ding, H., Dadap, J. I., Xing, H. G. & Osgood, R. M. Electronic Structure of the Metastable Epitaxial Rock-Salt SnSe {111} Topological Crystalline Insulator. *Phys. Rev. X* **7**, 041020 (2017).
14. Katase, T., Takahashi, Y., He, X., Tadano, T., Ide, K., Yoshida, H., Kawachi, S., Yamaura, J., Sasase, M., Hiramatsu, H., Hosono, H. & Kamiya, T. Reversible 3D-2D structural phase transition and giant electronic modulation in nonequilibrium alloy semiconductor, lead-tin-selenide. *Sci. Adv.* **7**, eabf2725 (2021).
 15. Cho, S., Kim, S., Kim, J. H., Zhao, J., Seok, J., Keum, D. H., Baik, J., Choe, D.-H., Chang, K. J., Suenaga, K., Kim, S. W., Lee, Y. H. & Yang, H. Phase patterning for ohmic homojunction contact in MoTe₂. *Science* **349**, 625–628 (2015).
 16. Bradlyn, B., Elcoro, L., Cano, J., Vergniory, M. G., Wang, Z., Felser, C., Aroyo, M. I. & Bernevig, B. A. Topological quantum chemistry. *Nature* **547**, 298–305 (2017).
 17. Sie, E. J., Nyby, C. M., Pemmaraju, C. D., Park, S. J., Shen, X., Yang, J., Hoffmann, M. C., Ofori-Okai, B. K., Li, R., Reid, A. H., Weathersby, S., Mannebach, E., Finney, N., Rhodes, D., Chenet, D., Antony, A., Balicas, L., Hone, J., Devereaux, T. P., Heinz, T. F., Wang, X. & Lindenberg, A. M. An ultrafast symmetry switch in a Weyl semimetal. *Nature* **565**, 61–66 (2019).
 18. Zhang, M. Y., Wang, Z. X., Li, Y. N., Shi, L. Y., Wu, D., Lin, T., Zhang, S. J., Liu, Y. Q., Liu, Q. M., Wang, J., Dong, T. & Wang, N. L. Light-Induced Subpicosecond Lattice Symmetry Switch in MoTe₂. *Phys. Rev. X* **9**, 021036 (2019).
 19. Vaswani, C., Wang, L.-L., Mudiyansele, D. H., Li, Q., Lozano, P. M., Gu, G. D., Cheng, D., Song, B., Luo, L., Kim, R. H. J., Huang, C., Liu, Z., Mootz, M., Perakis, I. E., Yao, Y., Ho, K. M. & Wang, J. Light-Driven Raman Coherence as a Nonthermal Route to Ultrafast Topology Switching in a Dirac Semimetal. *Phys. Rev. X* **10**, 021013 (2020).
 20. Luo, L., Cheng, D., Song, B., Wang, L.-L., Vaswani, C., Lozano, P. M., Gu, G., Huang, C., Kim, R. H. J., Liu, Z., Park, J.-M., Yao, Y., Ho, K., Perakis, I. E., Li, Q. & Wang, J. A light-induced phononic symmetry switch and giant dissipationless topological photocurrent in ZrTe₅. *Nat. Mater.* **20**, 329–334 (2021).
 21. Mogi, M., Choi, D., Primeau, L., Lv, B., Azoury, D., Su, Y., Fu, L., Zhang, Y. & Gedik, N. Direct Observation of a Photoinduced Topological Phase Transition in Bi-Doped (Pb,Sn)Se. *Phys. Rev. Lett.* **133**, 236601 (2024).
 22. Zhao, L.-D., Lo, S.-H., Zhang, Y., Sun, H., Tan, G., Uher, C., Wolverton, C., Dravid, V. P.

- & Kanatzidis, M. G. Ultralow thermal conductivity and high thermoelectric figure of merit in SnSe crystals. *Nature* **508**, 373–377 (2014).
23. Li, C. W., Hong, J., May, A. F., Bansal, D., Chi, S., Hong, T., Ehlers, G. & Delaire, O. Orbitally driven giant phonon anharmonicity in SnSe. *Nat. Phys.* **11**, 1063–1069 (2015).
 24. Chattopadhyay, T., Pannetier, J. & Von Schnering, H. G. Neutron diffraction study of the structural phase transition in SnS and SnSe. *J. Phys. Chem. Solids* **47**, 879–885 (1986).
 25. Wei, P.-C., Bhattacharya, S., Liu, Y.-F., Liu, F., He, J., Tung, Y.-H., Yang, C.-C., Hsing, C.-R., Nguyen, D.-L., Wei, C.-M., Chou, M.-Y., Lai, Y.-C., Hung, T.-L., Guan, S.-Y., Chang, C.-S., Wu, H.-J., Lee, C.-H., Li, W.-H., Hermann, R. P., Chen, Y.-Y. & Rao, A. M. Thermoelectric Figure-of-Merit of Fully Dense Single-Crystalline SnSe. *ACS Omega* **4**, 5442–5450 (2019).
 26. Jiang, B., Neu, J., Olds, D., Kimber, S. A. J., Page, K. & Siegrist, T. The curious case of the structural phase transition in SnSe insights from neutron total scattering. *Nat. Commun.* **14**, 3211 (2023).
 27. Sun, Y., Zhong, Z., Shirakawa, T., Franchini, C., Li, D., Li, Y., Yunoki, S. & Chen, X.-Q. Rocksalt SnS and SnSe: Native topological crystalline insulators. *Phys. Rev. B* **88**, 235122 (2013).
 28. Hsieh, T. H., Lin, H., Liu, J., Duan, W., Bansil, A. & Fu, L. Topological crystalline insulators in the SnTe material class. *Nat. Commun.* **3**, 982 (2012).
 29. Dziawa, P., Kowalski, B. J., Dybko, K., Buczko, R., Szczerbakow, A., Szot, M., Łusakowska, E., Balasubramanian, T., Wojek, B. M., Berntsen, M. H., Tjernberg, O. & Story, T. Topological crystalline insulator states in $\text{Pb}_{1-x}\text{Sn}_x\text{Se}$. *Nat. Mater.* **11**, 1023–1027 (2012).
 30. Tanaka, Y., Ren, Z., Sato, T., Nakayama, K., Souma, S., Takahashi, T., Segawa, K. & Ando, Y. Experimental realization of a topological crystalline insulator in SnTe. *Nat. Phys.* **8**, 800–803 (2012).
 31. Huang, Y., Yang, S., Teitelbaum, S., De la Peña, G., Sato, T., Chollet, M., Zhu, D., Niedziela, J. L., Bansal, D., May, A. F., Lindenberg, A. M., Delaire, O., Reis, D. A. & Trigo, M. Observation of a Novel Lattice Instability in Ultrafast Photoexcited SnSe. *Phys. Rev. X* **12**, 011029 (2022).
 32. Zhou, J., Zhang, S. & Li, J. Normal-to-topological insulator martensitic phase transition in group-IV monochalcogenides driven by light. *NPG Asia Mater.* **12**, 1–9 (2020).
 33. Mocatti, S., Marini, G. & Calandra, M. Light-Induced Nonthermal Phase Transition to the

- Topological Crystalline Insulator State in SnSe. *J. Phys. Chem. Lett.* **14**, 9329–9334 (2023).
34. Han, Y., Yu, J., Zhang, H., Xu, F., Peng, K., Zhou, X., Qiao, L., Misochko, O. V., Nakamura, K. G., Vanacore, G. M. & Hu, J. Photoinduced Ultrafast Symmetry Switch in SnSe. *J. Phys. Chem. Lett.* **13**, 442–448 (2022).
35. Okawa, M., Akabane, Y., Maeda, M., Tan, G., Zhao, L.-D., Kanatzidis, M. G., Suzuki, T., Watanabe, M., Xu, J., Ren, Q., Fujisawa, M., Kanai, T., Itatani, J., Shin, S., Okazaki, K., Saini, N. L. & Mizokawa, T. Direct observation of multiple conduction-band minima in high-performance thermoelectric SnSe. *Scr. Mater.* **223**, 115081 (2023).
36. Li, J., Qi, Y., Yang, Q., Yue, L., Yao, C., Chen, Z., Meng, S., Xiang, D. & Cao, J. Femtosecond Electron Diffraction Reveals Local Disorder and Local Anharmonicity in Thermoelectric SnSe. *Adv. Mater.* **36**, 2313742 (2024).
37. Dringoli, B. J., Sutton, M., Luo, Z., Kanatzidis, M. G. & Cooke, D. G. Ultrafast Photoinduced Phase Change in SnSe. *Phys. Rev. Lett.* **132**, 146901 (2024).
38. Xia, Y., Qian, D., Hsieh, D., Wray, L., Pal, A., Lin, H., Bansil, A., Grauer, D., Hor, Y. S., Cava, R. J. & Hasan, M. Z. Observation of a large-gap topological-insulator class with a single Dirac cone on the surface. *Nat. Phys.* **5**, 398–402 (2009).
39. Sie, E. J., Rohwer, T., Lee, C. & Gedik, N. Time-resolved XUV ARPES with tunable 24–33 eV laser pulses at 30 meV resolution. *Nat. Commun.* **10**, 3535 (2019).
40. Wang, C. W., Xia, Y. Y. Y., Tian, Z., Jiang, J., Li, B. H., Cui, S. T., Yang, H. F., Liang, A. J., Zhan, X. Y., Hong, G. H., Liu, S., Chen, C., Wang, M. X., Yang, L. X., Liu, Z., Mi, Q. X., Li, G., Xue, J. M., Liu, Z. K. & Chen, Y. L. Photoemission study of the electronic structure of valence band convergent SnSe. *Phys. Rev. B* **96**, 165118 (2017).
41. Wang, Y. H., Steinberg, H., Jarillo-Herrero, P. & Gedik, N. Observation of Floquet-Bloch States on the Surface of a Topological Insulator. *Science* **342**, 453–457 (2013).
42. Kronik, L. & Shapira, Y. Surface photovoltage phenomena: theory, experiment, and applications. *Surf. Sci. Rep.* **37**, 1–206 (1999).
43. Zhang, P., Richard, P., Qian, T., Xu, Y.-M., Dai, X. & Ding, H. A precise method for visualizing dispersive features in image plots. *Rev. Sci. Instrum.* **82**, 043712 (2011).
44. Tanaka, Y., Sato, T., Nakayama, K., Souma, S., Takahashi, T., Ren, Z., Novak, M., Segawa, K. & Ando, Y. Tunability of the k-space location of the Dirac cones in the topological crystalline insulator $\text{Pb}_{1-x}\text{Sn}_x\text{Te}$. *Phys. Rev. B* **87**, 155105 (2013).
45. Huang, Y., Teitelbaum, S., Yang, S., De la Peña, G., Sato, T., Chollet, M., Zhu, D., Niedziela, J. L., Bansal, D., May, A. F., Lindenberg, A. M., Delaire, O., Trigo, M. & Reis, D. A.

- Nonthermal Bonding Origin of a Novel Photoexcited Lattice Instability in SnSe. *Phys. Rev. Lett.* **131**, 156902 (2023).
46. Wall, S., Yang, S., Vidas, L., Chollet, M., Glowina, J. M., Kozina, M., Katayama, T., Henighan, T., Jiang, M., Miller, T. A., Reis, D. A., Boatner, L. A., Delaire, O. & Trigo, M. Ultrafast disordering of vanadium dimers in photoexcited VO₂. *Science* **362**, 572–576 (2018).
 47. Sternbach, A. J., Slusar, T., Ruta, F. L., Moore, S., Chen, X., Liu, M. K., Kim, H. T., Millis, A. J., Averitt, R. D. & Basov, D. N. Inhomogeneous Photosusceptibility of VO₂ Films at the Nanoscale. *Phys. Rev. Lett.* **132**, 186903 (2024).
 48. Kooi, B. J. & Wuttig, M. Chalcogenides by Design: Functionality through Metavalent Bonding and Confinement. *Adv. Mater.* **32**, 1908302 (2020).
 49. Guo, Z., Gu, H., Yu, Y., Wei, Z. & Liu, S. Broadband and Incident-Angle-Modulation Near-Infrared Polarizers Based on Optically Anisotropic SnSe. *Nanomaterials* **13**, 134 (2023).
 50. Kresse, G. & Furthmüller, J. Efficient iterative schemes for ab initio total-energy calculations using a plane-wave basis set. *Phys. Rev. B* **54**, 11169–11186 (1996).
 51. Kresse, G. & Joubert, D. From ultrasoft pseudopotentials to the projector augmented-wave method. *Phys. Rev. B* **59**, 1758–1775 (1999).
 52. Blöchl, P. E. Projector augmented-wave method. *Phys. Rev. B* **50**, 17953–17979 (1994).
 53. Perdew, J. P., Burke, K. & Ernzerhof, M. Generalized Gradient Approximation Made Simple. *Phys. Rev. Lett.* **77**, 3865–3868 (1996).
 54. Pizzi, G., Vitale, V., Arita, R., Blügel, S., Freimuth, F., Géranton, G., Gibertini, M., Gresch, D., Johnson, C., Koretsune, T., Ibañez-Azpiroz, J., Lee, H., Lihm, J.-M., Marchand, D., Marrazzo, A., Mokrousov, Y., Mustafa, J. I., Nohara, Y., Nomura, Y., Paulatto, L., Poncé, S., Ponweiser, T., Qiao, J., Thöle, F., Tsirkin, S. S., Wierzbowska, M., Marzari, N., Vanderbilt, D., Souza, I., Mostofi, A. A. & Yates, J. R. Wannier90 as a community code: new features and applications. *J. Phys. Condens. Matter* **32**, 165902 (2020).
 55. Wu, Q., Zhang, S., Song, H.-F., Troyer, M. & Soluyanov, A. A. WannierTools: An open-source software package for novel topological materials. *Comput. Phys. Commun.* **224**, 405–416 (2018).

Methods

Sample synthesis.

The SnSe and (Pb,Sn)Se thin films were epitaxially grown on semi-insulating InP(100) substrates ($>5\times 10^6 \Omega\cdot\text{cm}$) in our custom-built molecular beam epitaxy (MBE) chamber ($<1\times 10^{-7}$ torr) at a growth temperature of 175°C . The substrates were pre-annealed at 340°C in the growth chamber prior to growth. Beam fluxes were calibrated using a quartz crystal microbalance, with an excess flux of Se, approximately twice that of Sn and Pb, to suppress Se vacancies. The film growth rate was about 0.5 nm min^{-1} , calibrated by X-ray reflectivity measurements. The typical thickness of our samples is about 50 nm, a thickness comparable to the optical penetration depth at our pump wavelength of 1030 nm (1.2 eV)⁴⁹. After growth, the samples were cooled to approximately 100°C under a continued supply of Se flux, then transferred to the ARPES chamber ($<1\times 10^{-10}$ torr) directly connected to the MBE chamber through a preparation chamber ($<5\times 10^{-10}$ torr) without exposure to the atmosphere. To avoid charging the samples on the insulating substrates, they were electrically grounded by placing the tip of a tungsten wire on the sample, which was connected to the sample holder.

trARPES.

In our trARPES setup, a Yb fiber laser (Tangerine, Amplitude) provides fundamental beam pulses with a center wavelength of 1030 nm (1.2 eV), a duration of 135 fs, a pulse energy of 250 μJ , and a repetition rate of 300 kHz. The fundamental beam is divided into two branches for the pump and probe beams. In the probe branch, to generate extreme ultraviolet (XUV) beams, the second or third harmonic is generated through $\beta\text{-BaB}_2\text{O}_4$ crystals and is focused on Ar gas ejected from a gas-jet nozzle. To select the desired harmonics, such as 10.8 eV and 21.6 eV, we use an off-plane mounted grating in the XUV monochromator (McPherson Inc.), which eliminates the copropagating seed beam and other harmonics³⁹. Subsequently, a toroidal mirror focuses the XUV beams on the samples. The polarization of the probe beams was linear vertical polarization. In the pump branch, the fundamental beam is sent to an optical parametric

amplifier (Orpheus-HP, Light Conversion) to convert the wavelength to 800 nm (1.55 eV). The pump polarization was linear horizontal polarization. The data for linear vertical polarization is shown in Supplementary Section 2.

An angle-resolved time-of-flight (ARTOF) analyzer (ARTOF 10k, ScientaOmicron) was used to collect the emitted photoelectrons. To locate the Brillouin zone edge of SnSe in the area of the photoelectron detector for our probe photon energies, we tilted the sample by approximately 42° for 10.8 eV and 22° for 21.6 eV from the flat condition. The pump and probe beams are nearly collinear, with an incident angle of about 45° . The incident angles of the pump and probe beams relative to the sample are approximately 3° and 23° for 10.8 eV and 21.6 eV, respectively. Our energy resolution, which combines the resolutions of our pump, probe beams, and detector, and the estimated upper bound of the time resolution for the present study are approximately 50 meV and 420 fs, respectively (Supplementary Section 2). Curvature plots were used to highlight the transient dispersive bands, as presented in Fig. 3.

DFT calculations.

Density-functional theory (DFT) calculations were performed using the Vienna ab initio Simulation Package (VASP) with the projector-augmented wave (PAW) method^{50–52}. The exchange-correlation functional was treated using the generalized gradient approximation (GGA) parametrized by Perdew-Burke-Ernzerhof (PBE)⁵³. The kinetic energy cutoff for the plane-wave basis was set to 300 eV. The Brillouin zone integration was carried out using a $4 \times 12 \times 12$ Γ -centered k-point mesh for the Pnma and Cmcm phases ($a = 11.52 \text{ \AA}$) and a $12 \times 12 \times 12$ Γ -centered k-point mesh for the Immm phase ($a = 5.76 \text{ \AA}$). Maximally localized Wannier functions (MLWFs) for Sn-5s, 5p, and Se-4p orbitals were constructed using the WANNIER90 package⁵⁴. Surface and edge state calculations, based on the maximally localized Wannier functions, were performed using the WannierTools package⁵⁵.

trXRD.

Pump-probe hard x-ray diffraction experiments were carried out at the BL3 EH2 of the SPring-8 Angstrom Compact free electron LAser (SACLA), an x-ray-free electron laser facility in Japan. The probe consisted of 10 keV x-ray pulses with a duration of approximately 10 fs (full width at half maximum, FWHM). These pulses were focused through compound refractive lenses (CRL) to a spot size of approximately $28.5 \mu\text{m} \times 29.3 \mu\text{m}$ in diameter (FWHM) and were incident at a grazing angle of 3.0° relative to the sample surface. The pump comprised a time-delayed 1.55 eV (797.7 nm) beam with a duration of about 30 fs (FWHM). The incidence angle of the pump beam varies as different Bragg peaks were measured, ranging from 6.9° to 8.9° with respect to the sample surface. The pump spot size was approximately $623.3 \mu\text{m} \times 654.5 \mu\text{m}$ (FWHM). Measurements were performed using a Huber diffractometer, and x-ray scattering images were acquired with a 2D multiport charge-coupled device (MPCCD) detector. Both the 10 keV x-ray probe and the 1.55 eV infra-red (IR) pump pulses were linearly polarized (horizontal to the ground) and operated at a repetition rate of 30 Hz. All measurements started from the Bragg condition and were performed under the ambient condition.

Dynamics of transient topological crystalline order.

To further explore the temporal evolution of the photoinduced topological state, we conducted time-resolved measurements on the SnSe film grown on a PbSe(100) buffer layer (sample #2). Extended Data Fig. 1a displays a series of energy-momentum snapshots around the \bar{Z} point, along with curvature analyses. Consistent with the results from sample #1 (Fig. 2b), a Dirac-like band dispersion appears as early as 0.2 ps, and can be detected at $\Delta t = 0$ ps, likely due to temporal broadening pump and/or probe pulses, and then disappears within ~ 5 ps.

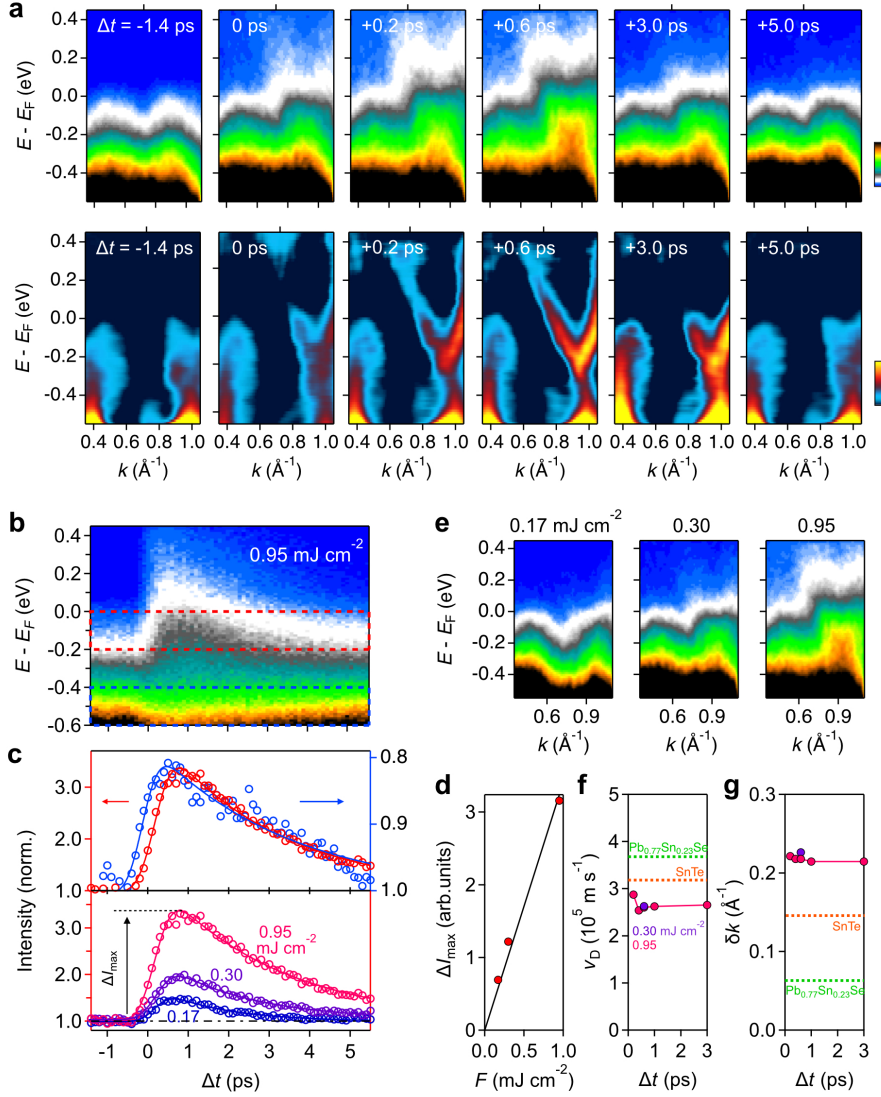
The evolution of the spectral intensity around the \bar{Z} point is shown in Extended Data

Fig 1b. After photoexcitation, intensity near E_F (red square) is enhanced, indicating the formation of an in-gap band, while the valence-band intensity (blue square) is suppressed. The integrated intensities of these red and blue regions are plotted in Extended Data Fig. 1c (top). Notably, the buildup of the in-gap state is slightly delayed (~ 0.3 ps) relative to the depletion of the valence band, whereas the recovery of the valence-band intensity and the decay of the in-gap band proceed in parallel. These temporal profiles fit well to an exponential decay model: $\Delta I(t) = [I_{\text{peak}} \exp(-\frac{t-t_0}{\tau}) \cdot \{1 + \text{erf}(\frac{2\sqrt{2}(t-t_0)}{w})\}] * g(w_0, t)$, where I_{peak} , t_0 , τ , erf , g , w , and w_0 are the peak intensity, time zero, decay time, error function, Gaussian function, system response time, and Gaussian temporal width, respectively. This behavior is consistent with a carrier-density-driven process: electron-hole photoinjection initiates the phase transition followed by phonon-mediated structural reorganization that stabilizes the in-gap Dirac bands.

We next examined the fluence dependence of this transient state. As shown in Extended Data Fig. 1c (bottom) and Fig. 1d, the in-gap band intensity increases linearly with pump fluence up to ~ 0.95 mJ/cm², confirming that the photoexcited carrier density is a key factor in driving the topological transition.

Finally, we investigated how pump fluence affects both the Dirac dispersion and its temporal evolution. Extended Data Fig. 1e demonstrates that the Dirac dispersion becomes clearer at higher pump fluences. In Extended Data Fig. 1g,h, we summarize the temporal dynamics of the in-gap Dirac band dispersion, showing that neither the Dirac velocity (v_D) nor the separation of the Dirac point from the \bar{Z} point (δk) changes significantly with time and fluence. The dispersion thus appears rigid under these photoexcitation conditions. Such rigidity suggests that the photoinduced change to the Immm-like structure proceeds locally, in contrast to the gradual atomic displacements toward Immm, as studied by our DFT calculations (Supplementary Section 5).

Data availability. All relevant data within this paper are available from the authors.



Extended Data Fig. 1 | Dynamics of transient topological crystalline order. **a**, Snapshots of energy-momentum cuts (top) and curvature plots (bottom) along k_z at $k_y = 0 \text{ \AA}^{-1}$ near the \bar{Z} point at various time delays. **b**, Time evolution of trARPES intensity integrated around the \bar{Z} point. **c**, Time evolution of spectral weights below the Fermi level. Red ($-0.1 \pm 0.1 \text{ eV}$) and blue ($-0.5 \pm 0.1 \text{ eV}$) boxes highlight the energy regions of interest. Top panel compares normalized intensities for the red and blue regions at a pump fluence of 0.95 mJ/cm^2 . Bottom panel shows intensity for selected pump fluences, integrated over the red region. Intensities are normalized to their values at $\Delta t = -1.4 \text{ ps}$. Solid curves represent fits to a single-exponential decay model

(see Methods). **d**, Fluence dependence of the maximum intensity change (ΔI_{\max}), obtained by subtracting the intensity at $\Delta t = -1.4$ ps from the peak intensity. The black line is a linear fit. **e**, trARPES band structure maps around the \bar{Z} point for selected pump fluences at $\Delta t = +0.6$ ps. **f,g**, Time evolution of the Dirac velocity (v_D) (**f**) and momentum shift of the Dirac point relative to the \bar{Z} point (δk) (**g**) for pump fluences of 0.30 mJ/cm^2 and 0.95 mJ/cm^2 . These values are compared with those for $\text{Pb}_{0.77}\text{Sn}_{0.23}\text{Se}$ (see Fig. 3d, inset) and SnTe (ref. ⁴⁴).